



Article

Sparse Tiled Planar Array: The Shared Multibeam Aperture for Millimeter-Wave Joint Communication and Sensing

Hadi Alidoustaghdam , André Kokkeler  and Yang Miao 

Faculty of Electrical Engineering, University of Twente, 7522 NB Enschede, The Netherlands; a.b.j.kokkeler@utwente.nl (A.K.); y.miao@utwente.nl (Y.M.)

* Correspondence: hadi.alidoustaghdam@utwente.nl

Abstract: Multibeam planar arrays are investigated as shared apertures for dual functionality in millimeter-wave (mmWave) joint communication and sensing (JCAS), providing time division duplex communication and full-duplex sensing with steerable beams. The conventional uniform planar arrays (CUPA)s have limited angular resolution, whereas the sparse planar arrays (SPA)s are often very costly to implement. In order to have a low-cost aperture with high angular resolution, we propose to design a sparse tiled planar array (STPA) shared aperture. Our proposed solution is modular tiling and uniform at the subarray level but sparse at the aperture level. The modular tiling and sparse design of a planar array are non-convex optimization problems; however, we exploit the fact that the more irregularity of the antenna array geometry, the less the side lobe level (SLL). In a JCAS scenario, we compare the performance of STPA, CUPA, and SPA, regarding the *spectral efficiency* of a line-of-sight (LoS) included communication link, *detection loss rate*, and *detection accuracy rate* for sensing, and the *blockage time* in case of an overlapping communication and sensing beam. The SPA for comparison has the same size and beamwidth as STPA, but less average SLL and less modular design. The results show that the same spectral efficiency is achieved in the communication link for CUPA, SPA, and STPA. The effect of a smaller beamwidth of the STPA and SPA is reflected in the lower detection loss rate of them compared to that of the CUPA, but the side lobes of these sparse solutions result in errors in the association of the detected and true targets and hence a reduction in the detection accuracy. In such a multibeam solution for JCAS, it is critical to study blockage time, and we show that the STPA and SPA have a 40% shorter blockage time compared to the CUPA when a blocker moves across the LoS of the communication link. Therefore, STPA is a trade-off solution between CUPA and SPA, since it has uniformly distributed antennas within the subarrays as in CUPA, but a sparse solution in the whole aperture as in SPA, which guarantees the same beamwidth and sensing performances as a SPA.

Keywords: 6G; joint communication and sensing; shared aperture; multibeam; tiled planar array; sparse array; spectral efficiency; blockage duration; target detection; angle-of-arrival



Citation: Alidoustaghdam, H.; Kokkeler, A.; Miao, Y. Sparse Tiled Planar Array: The Shared Multibeam Aperture for Millimeter-Wave Joint Communication and Sensing. *Electronics* **2023**, *12*, 3115. <https://doi.org/10.3390/electronics12143115>

Academic Editor: Dimitra I. Kaklamani

Received: 26 May 2023

Revised: 6 July 2023

Accepted: 12 July 2023

Published: 18 July 2023



Copyright: © 2023 by the authors. Licensee MDPI, Basel, Switzerland. This article is an open access article distributed under the terms and conditions of the Creative Commons Attribution (CC BY) license (<https://creativecommons.org/licenses/by/4.0/>).

1. Introduction

In the migration to 6G and connected smart networks, communication and sensing devices have to be integrated to maintain the reliability of high data-rate connectivity and to have accurate information on the surrounding operating environment [1]. There are many open challenges for joint communication and sensing (JCAS), especially for the co-design of communication and radar sensing functionality within a single physical array aperture. For example, what (shared) waveform to use, what shared array aperture configuration, and how to optimize the resource allocation, are all open to be resolved with effectiveness and efficiency [1–4]. In this paper, our interest lies in the base station (BS) array configuration design—a shared aperture—to optimize the JCAS performance.

Conventionally, the free-space radiation parameters, i.e., directivity, half-power beamwidth, and side lobe level (SLL) were the figure-of-merits for designing antenna

arrays. These free-space radiation parameters are valid for the radio propagation channels with a dominant line-of-sight (LoS) path. However, in case of channels with considerable non-line-of-sight (NLoS) paths, for multi-user multiple-input-multiple-output (MU-MIMO) communications and in a dense mmWave networks [5], the spectral efficiencies of communication links are the reliable performance metrics [6,7]. Therefore, for an optimal end-to-end communication performance, the beamforming vector applied on the antennas at the BS, and consequently the radiation pattern, shall be determined by the channel dynamics and be configured for maximizing the spectral efficiency of communication links. The optimized BS radiation pattern could be with a narrow or wide beamwidth and single or multi beams. Additionally, the favorable channel of a phased array radar, particularly in millimeter-waves (mmWave)s, is with a dominant reflected (backscattered) path, thus a single beam with low SLL and narrow beamwidth focusing towards the scatterer is always beneficial for improving the signal-to-noise ratio (SNR) and cross-range resolution [8].

To enable JCAS, a dynamic radiation pattern at the BS is desired, as either communication or sensing might dictate to react to the dynamic channel conditions. To enable a dynamic radiation pattern, antenna selection, which involves synthetic changes in aperture size and geometry [9], may be necessary.

In the presence of a LoS communication link and the direct illumination of the sensing target, which is the case of study in this paper, instead of antenna selection and synthetic aperture change, the use of all antenna elements in the BS is beneficial for increasing the SNR and hence the performance of JCAS. It is stated in Ref. [10] that increasing the size of the aperture while preserving the same antenna numbers did not improve the directivity, but decreased the beamwidth. Therefore, we focus on designing a shared array aperture for JCAS with a low SLL and narrow beamwidth, given a fixed aperture size. We also focus on maintaining an appropriate number of radiating elements to reduce the system cost and space requirements. In order to manage the number of array elements and at the same time enhancing the performance of communication and sensing, we explore solutions incorporating array tiling [6,7,11–14], sparse arrays [15], and modular design [10]. These goals are studied in Ref. [16], where a reconfigurable mmWave antenna array platform based on antenna tiles was studied and implemented for the communication applications. Therefore, this paper extends those modular tiling solutions to the JCAS scenarios by a sparse subarray design.

1.1. State-of-the-Art of Large Antenna Array for Communication or Sensing

1.1.1. Array Tiling

By grouping antennas into the so-called “tiles” and feeding each tile with one phase shifter, it guarantees a large aperture with a reduced number of phase shifters, reducing the hardware costs. Until now, the investigations on array tiling and the discussions on the resultant performance were mainly for phased array communications [11–14] or massive MIMO communications [6,7]. The genetic algorithm [17,18], iterative convex programming or information-theoretic entropy concepts were used for tiling the array in a (near-)optimal manner. Among these solutions, the authors in Ref. [11] have proposed that two adjacent antennas can be excited by the same phase shifter, which is hence regarded as one domino tile. If the phase centers of these dominoes are distributed with maximum entropy in the aperture, the radiation pattern has a low SLL.

1.1.2. Sparse Modular Subarray

A narrow beamwidth of the radiation pattern of a phased array requires a large array aperture size. To decrease the complexity of a large aperture, sparse modular arrays were studied in Ref. [10] where the positions of the modular uniform subarrays were optimized for the desired beamwidth and SLL. When sparse arrays are considered, clustering antennas is another solution to avoid the complexity of transmission lines from the RF front-end to antennas. For instance, in Refs. [19,20], the BS antenna array was designed based on irregular clustering and sequential rotation, where the optimization problem considered

the inter-element spacing, aperture size, and modular layout design. Due to a large transmission distance in satellite communications, a larger aperture is desirable to lower beamwidth, therefore the solutions for the apertures in non-terrestrial or aerial-terrestrial communications are a source of inspiration for designing JCAS BS in this paper. For instance, sparse subarrays are proposed in satellite-terrestrial integrated networks [21]. In non-terrestrial networks, a sunflower sparse array of uniform hexagonal subarrays was designed for satellite applications in Refs. [15,22].

Depending on whether separating [23] or sharing waveforms [24] between communication and sensing, the requirements for JCAS apertures are different, as in, e.g., the number and locations of antennas and the interference mitigation. In case of the presence of a dominant LoS path or a reflected path with high SNR, a sparse large array is beneficial for better angle-of-arrival (AoA) estimation [8,10]. We intend to exploit the solutions mentioned above to design a novel large JCAS shared aperture with an affordable number of phase shifters.

1.2. The Contributions of This Paper

As a solution for BSs, we propose a shared aperture for JCAS, as well as an auxiliary aperture for radar full-duplex operation with a shared waveform. The proposed BS aperture performs in time-division duplexing (TDD) downlink communication and monostatic sensing at the duration of TDD-downlink, and uplink communication and monostatic sensing at the duration of TDD-uplink. The proposed shared aperture for JCAS is a sparse tiled planar array (STPA). Firstly, a large aperture with uniformly distributed antennas is tiled by dominoes based on the maximum entropy of tile centers in the aperture. The sunflower array is then exploited to locate the center of subarrays and lower the number of tiles. When the tiles in subarrays are chosen, the positions of the subarrays are optimized to lower SLL. A comparison of the designed STPA to a conventional uniform planar array (CUPA) and a sunflower sparse planar array (SPA) with the same number of antennas is provided. The employed SPA for comparison has the same aperture size and the same beamwidth as the STPA, but, due to higher freedom in the location of its elements, it has less average SLL and a less modular design. The main contributions of this paper are three-fold.

- **Array configuration:** In the literature, a JCAS array is communication-centric, as a CUPA is employed in the TDD-downlink [23] or TDD-uplink [25] JCAS. Knowing that a CUPA has a larger beamwidth and is not optimal for sensing, in this paper, an STPA is proposed for JCAS at the BS since a narrow beamwidth of the transmit beam (in TDD-downlink) or receive beam (in TDD-uplink) is required for proper AoA estimation in sensing. This narrow beamwidth is profitable for increasing the number of beams for multi-user communication as well. The numerical results are provided for the duration of TDD-downlink, however, STPA can be adopted for TDD-uplink and monostatic sensing at the BS by the method in Ref. [26]. Considering the large bandwidth in JCAS at, e.g., 5G NR FR2, the irregularity introduced by tiling and sparse subarray geometries, compared to the conventional uniform arrays, results in a low SLL in the radiation pattern over a larger frequency band [27]. The numerical results show that STPA has a proper SLL when the frequency is scaled up to 1.625 times the desired frequency of operation, which results in a 42% increase in the operational frequency of the array compared to the CUPA. A comparison of STPA to SPA shows that SPA is applicable for a wider band, although with slightly higher SLL and more irregularity in the aperture. However, the STPA is uniform array at the subarray level, making it easier to manufacture compared to SPA.
- **Sensing performance:** The angular resolution of the JCAS aperture is improved by suitable adjustment of tiling and sparse design. As stated in Ref. [11], the tiled array has the benefits of modular design and lower SLL in wider scanning angles compared to a solely sparse design. The narrow beamwidth of the proposed STPA compared to CUPA ensures illuminating and receiving from only the desired angle during TDD-downlink and TDD-uplink monostatic sensing at the BS, respectively.

The narrow beamwidth is achieved at the cost of a higher SLL compared to a CUPA, and the effect of this drawback is observed in the resulting error in the detection accuracy of targets.

- **JCAS performance:** The narrow beamwidth of STPA is beneficial for decreasing the blockage time in a JCAS scenario, since the spectral efficiency is dropped when the blocker reaches the narrower communication beam, i.e., we show in a JCAS scenario that if a tracked target moves towards the boresight of aperture and blocks the communication link, the designed STPA can have a 40% shorter blockage time than a CUPA.

The following notations are used in this paper: $(\cdot)^T$ and $(\cdot)^*$ denote the transpose and conjugate transpose operator, respectively. $\|\cdot\|_F$ is the Frobenius norm.

2. Proposed STPA Configuration for JCAS, Its Design Pipeline, and Performance

In this section, we present the proposed STPA configuration and its design pipeline. Note that the novelty in this paper lies in the novel combination of known techniques for producing a novel STPA multibeam solution for JCAS scenarios to study communication and sensing performances, and blockage time. First, we present the JCAS architecture and protocol that are used in this paper. Second, we present the proposed STPA array configuration and its design pipeline. Third, we present the communication and sensing performance with corresponding representative channel models.

2.1. Intro: JCAS Architecture and Protocol

Let us consider a BS based on a fully connected analog array, as in Figure 1. A JCAS aperture with N_{imi} antennas is supposed to communicate with a single user equipment (UE) in the TDD scheme and at the same time illuminate a sensing target by using two beams. The number of RF beams is determined by the number of RF chains, and when accompanied by digital beamforming, provides communication to multiple users. The interference among these users can be mitigated by generating narrow beams with low SLLs, and this demands a careful configuration of antenna arrays. Without loss of generality, we study the performance of only one RF chain and one user, since other RF chains, if needed for multiple users, are also connected to the same antennas. The JCAS aperture serves as the transmitter (Tx) during simultaneous downlink communication and monostatic sensing, and as the receiver (Rx) during simultaneous uplink communication and monostatic sensing. Due to long communication subframes (e.g., 1 ms for 5G NR at FR2) and the resulting radar sensing ‘dead zone’ of maximum 150 km using TDD, a full-duplex radar sensing functionality is mandatory for perpetual sensing of the surrounding environment. To this end, auxiliary apertures with N_{aux} antennas are needed to serve as the radar receiver during downlink communication and simultaneous monostatic sensing, and as radar transmitter during uplink communication and simultaneous monostatic sensing. The reason for having transmit antennas at the uplink is to address the limitations of sensing solely by the communication signal, i.e., the power resources of communication users are limited, which affects the SNR for sensing. Additionally, these users often have beamforming toward BS, which means that the environment is not illuminated for sensing. Furthermore the sensing environment depends on the user’s location, which may be unknown. Therefore, having transmit antennas at BS during uplink communication are beneficial for sensing [26]. The signal processing during downlink communication while monostatic sensing and during uplink communication while monostatic sensing are different: the backscattered signals from the sensing target and the uplink communication signal interfere at the shared aperture, which operates as a JCAS receiver. In such a case, interference cancellation techniques are needed to separate the signals. Downlink communication with simultaneous monostatic sensing does not encounter such interference, since the auxiliary Rx only receives the backscattered signal from the sensing target. In this paper, we focus on simultaneous downlink communication and monostatic sensing scenarios to demonstrate the performance of the proposed STPA. Nevertheless, the demonstrated performance is

representative of the uplink communication and simultaneous monostatic sensing, whereas the prerequisite interference cancellation is beyond the scope of this paper.

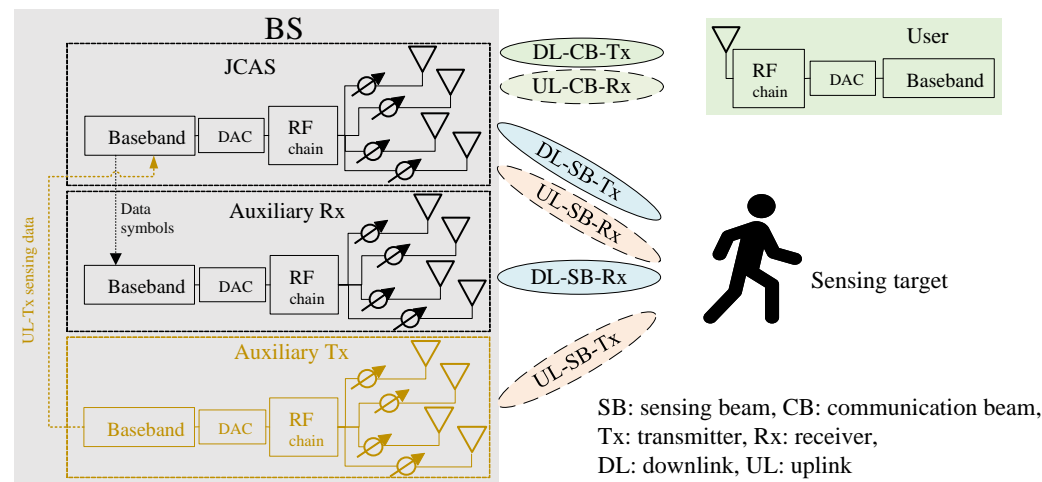


Figure 1. The configuration for JCAS in BS.

Both a bistatic communication link and a monostatic radar would benefit from narrow transmit and receive beam patterns to increase SNR. The challenging part is rather to situate multiple focusing beams in a single JCAS aperture, and then the auxiliary arrays can be designed accordingly. With a narrow communication and a narrow sensing beam from the shared JCAS aperture, the auxiliary Rx can have fewer antenna numbers to decrease the implementation costs, hence we assume $N_{ini} \gg N_{aux}$. Therefore, the tiling is targeted only to the N_{ini} antennas at the JCAS aperture, and we simply choose $N_{aux} = 1$ and focus on the JCAS aperture for the performance study of STPA. We use communication signals with orthogonal frequency division multiplexing (OFDM) waveforms to communicate and sense.

2.2. Proposed STPA and Its Design Pipeline

2.2.1. Design Objective for JCAS and the Proposed STPA

The objective is to design a shared aperture for JCAS operating in the band of n261 of 5G NR. It is shown in Figure 2 that θ is the elevation angle measured from z-axis and ϕ is the azimuth angle measured from the x-axis. The design objectives are: a center frequency of $f_c = 28$ GHz with 400 MHz bandwidth, the field of view (FoV) of 30° in the elevation and of 360° in the azimuth angles [14], symmetrical 3 dB-beamwidth of 10° in azimuth and elevation domain.

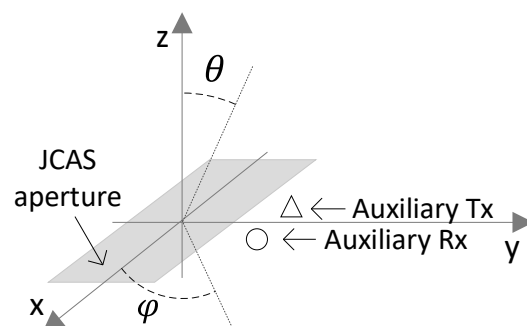


Figure 2. The configuration of antennas at the BS.

2.2.2. Design Pipeline

Note that the inherent problems of array tiling for the JCAS aperture in order to obtain the smallest SLL and a sparse irregular geometry for the accurate angle estimations are

problems of non-convex optimizations and are difficult to solve. Instead, we employ local optimizations based on the foreknowledge in two steps, as it is shown in the flowchart of Figure 3. The main idea of this proposed local optimization based design pipeline is based on two scales of irregularity, namely the phase centers of tiles in the whole aperture (global scale), and the geometry of subarrays (local scale).

- **Step 1: Global scale tiling.** Initially, a large CUPA is tiled for the minimum SLLs in the radiation pattern. The tiling problem is formulated based on maximum entropy in the distribution of the phase centers of the tiles in the array. In the schematic aperture shown in Figure 2, assume that N_{sub} antennas of JCAS aperture are grouped in tiles and fed by power dividers. The center of mass of such a tile could be considered as the center of phase for radiation from the whole tile. The irregularity in the distributions of these phase centers is measured with an information-theoretic entropy-based objective function, i.e., if the entropy of the phase centers at each row and column of the aperture is maximized, then the resulting phased array aperture has a desired SLL while scanning. To obtain more mathematical insight into tiling based on the maximum entropy, refer to Ref. [28].
- **Step 2: Local scale subarray irregularity.** The resultant tiled array can still be thinned by grouping some tiles in subarrays and removing others. A subarray is determined by a circle circumventing its tiles. The centers of these circles (subarrays) are obtained by the geometry of the sunflower array since the positions of elements are controllable, although it is an aperiodic sparse array (see Appendix A). Essentially, other deterministic sparse arrays, e.g., the circular array, could be utilized since this only performs as an initialization for the next convex optimization [29]. The radius of a circle is a thinning parameter for the aperture, which can be tuned to reach the desired SLL with a minimum number of tiles. It is assumed that the phase centers of tiles are still distributed with a maximum entropy after thinning of the aperture, but the inter-distances among subarrays increases the SLL, however, the resultant empty space between subarrays can be exploited to optimize the location of subarrays efficiently to decrease the SLL (see Appendix B).

When the JCAS aperture with the desired SLL and beamwidth is achieved, we compare its performance with conventional CUPA and SPA.

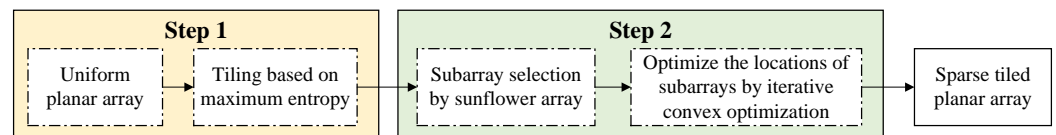


Figure 3. The flowchart of designing STPA.

2.2.3. Expanded Beam Pattern

The radiation field of an array with isotropically radiating elements in (u, v) -space can be obtained by:

$$f(u, v) = \frac{1}{N} \sum_{n=1}^N \alpha_n e^{j\Omega_n} e^{jk(ux_n + vy_n)}, u = \sin \theta \cos \phi, v = \sin \theta \sin \phi \tag{1}$$

where N is the number of radiating elements, and α_n and Ω_n are the amplitude and phase of excitation, respectively, $k = 2\pi/\lambda$ is the wave-number at the wavelength λ , and x_n and y_n are the positions of antennas in Cartesian coordinates. The radiation field in (1) can scan toward the angle $\Delta_g = (u_g, v_g)$ by the proper weighting of amplitudes and phases. In the case of conventional beamforming, which is based on only phase excitation in the elements, the weights are $\alpha_n = 1, \Omega_n = -jk(u_g x_n + v_g y_n)$. The radiation pattern is then as follows:

$$F(u, v; u_g, v_g) = \frac{1}{N^2} \left| \sum_{n=1}^N e^{jk((u-u_g)x_n + (v-v_g)y_n)} \right|^2 \tag{2}$$

In order to assure that the designed STPA bears the desired SLL and beamwidth in all scanning directions Δ_g s, the expanded beam pattern (EBP) is employed, as in Ref. [10]:

$$F_\zeta(\tilde{u}, \tilde{v}) = \frac{1}{N^2} \left| \sum_{n=1}^N e^{jk\zeta(\tilde{u}x_n + \tilde{v}y_n)} \right|^2, \zeta = 1 + \sin(\theta_{max}) \tag{3}$$

where $\tilde{u} = u - u_g, \tilde{v} = v - v_g$. The scanning of the beam in the whole $0^\circ \leq \theta \leq 90^\circ$ without grating lobes is not practical, therefore the desired angle of view is $0^\circ \leq \theta \leq \theta_{max}$ where θ_{max} is the maximum of angle θ . The SLL for $F_\zeta(\tilde{u}, \tilde{v})$ is studied to ensure an appropriate SLL in all scanning angles.

2.3. JCAS Scenarios and Performance Metrics

The performance metric for communication is spectral efficiency, which represents the number of bits transmitted per second in a specific bandwidth [30], and for sensing, the performance metric is angular resolution, which determines the smallest angle between two targets that are distinguishable for the radar [31]. The communication and sensing performances, as shown in Figure 4a–c, include cases without and with overlapping beams when the UE blocks the sensing link and also when the sensing target blocks the communication link. The overlapping occurs when:

$$(u_c - u_s)^2 + (v_c - v_s)^2 < r_b^2 \tag{4}$$

where (u_c, v_c) and (u_s, v_s) are the angles of communication and sensing beams, respectively, and r_b is the radius of the beamwidth in (u, v) -space. The user element may demonstrate some backscattering in reality, and a comprehensive study including the radar-cross-section of a user in a JCAS scenario is presented in Ref. [32], where the communication user is also the target for sensing. In pursuit of simplicity, we suppose that the user occupies only one range-angle bin and has a negligible reflection of electromagnetic waves. Additionally, we assume that the energy transmitted in the communication beam of the BS reaches the user after propagation loss and is captured by the user.

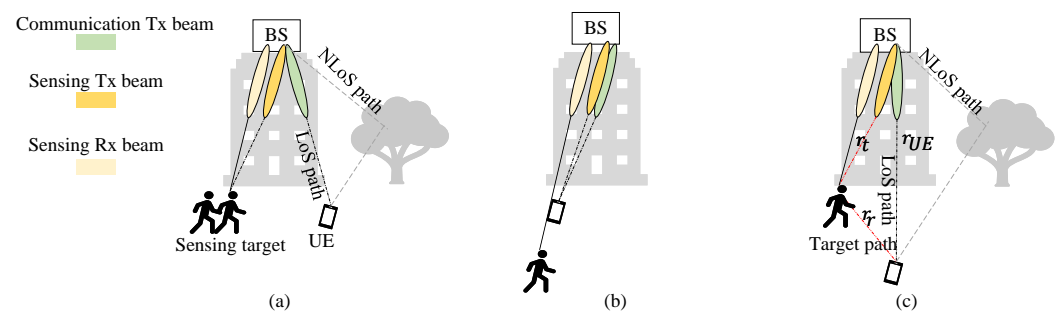


Figure 4. The scenarios for JCAS in downlink communication, (a) without overlapping of communication and sensing beams, (b) with overlapping of communication and sensing beams, when the UE blocks the sensing link, and (c) forthcoming overlapping of communication and sensing beams, when the sensing target can block the communication link.

2.3.1. JCAS Scenario 1: Non-Overlapping Communication and Sensing Beam Directions

Let us consider the scenario in Figure 4a. A geometric model for both communication and sensing is assumed to include L multipath signals with the angle-of-departure (AoD), $(\theta_{T,l}, \phi_{T,l})$ and angle-of-arrival (AoA), $(\theta_{R,l}, \phi_{R,l})$. The time-varying channel [33] can be expressed as:

$$\mathbf{H} = \sum_{l=1}^L b_l \delta(t - \tau_l) e^{j2\pi f_{D,l} t} \mathbf{a}_T(\theta_{T,l}, \phi_{T,l}) \mathbf{a}_R^T(\theta_{R,l}, \phi_{R,l}) \tag{5}$$

where b_l is the complex value modeling signal attenuation, τ_l is the propagation delay, and $f_{D,l}$ is the Doppler frequency. \mathbf{a}_T and \mathbf{a}_R are the steering vectors for transmit and receive arrays in the directions of multipath AoD and AoA, respectively. The channel (5) might also include the LoS path for communication. Note that $\mathbf{H} \in \mathbb{C}^{N_{JCAS} \times N_R}$, where N_{JCAS} denotes the number of radiating elements (either tiles or single-antennas) in the JCAS aperture, and N_R is the number of antennas in the receive aperture of the UE for the communication channel or the auxiliary aperture in BS for monostatic sensing.

The multibeam weighting vector at the JCAS aperture is [24]:

$$\mathbf{w}_{JCAS} = \sqrt{\rho}\mathbf{w}_c + \sqrt{(1-\rho)}\mathbf{w}_s \tag{6}$$

where $0 \leq \rho \leq 1$ is the power allocation factor between beams, which equals 0.5 in this paper. $\mathbf{w}_c \in \mathbb{C}^{N_{JCAS} \times 1}$ is the weighting vector for communication and is calculated by the right singular vector of the channel corresponding to the maximum singular value of \mathbf{H} with $\|\mathbf{w}_c\|_F^2 = 1$ [34]. $\mathbf{w}_s \in \mathbb{C}^{N_{JCAS} \times 1}$ denotes the weighting vector for sensing to a desired direction $\Delta_s = (\theta_s, \phi_s)$ and calculated by $\mathbf{w}_s = \mathbf{a}_T^*(\theta_s, \phi_s) / \|\mathbf{a}_T(\theta_s, \phi_s)\|_F$.

Communication Performance: We use spectral efficiency as the performance metric for communication. With Gaussian symbols transmitted in a mmWave channel, the spectral efficiency is [34]:

$$R = \log_2 \det \left(1 + \frac{\mathbf{H}^* \mathbf{w}_{JCAS}^* \mathbf{w}_{JCAS} \mathbf{H}}{\sigma_n^2} \right) \tag{7}$$

where σ_n^2 denotes the variance of a zero-mean Gaussian noise.

Sensing Performance: The main figure of merit of sensing in a JCAS scenario is the detection of targets as well as the angular-delay-Doppler estimates of targets. While the waveform configuration, including the subcarriers and bandwidth as well as symbol duration and the number of coherent processing symbols, determine the delay/range and Doppler estimates, respectively, the array configuration determines the accuracy and ambiguity of AoA/AoD estimates.

Assume that N_d OFDM symbols are required for a coherent processing interval for Doppler estimation. N_e and N_a are the number of elevation and azimuth angles, respectively, and $N_e \times N_a$ angles form a full sensing coverage. We suppose that self-interference is already canceled by a combination of passive [35] and active methods [26,36], therefore the received signal at the auxiliary Rx is simplified [24] to:

$$\begin{aligned} \tilde{y}_{n,n_a,q} &= \tilde{h}_{n,n_a,q} \tilde{s}_n + \tilde{z}_n, \\ \tilde{h}_{n,n_a,q} &= \sum_{l=1}^L b_l \mathbf{w}_{JCAS}^T \mathbf{a}_T(\theta_{T,l}, \phi_{T,l}) e^{-j2\pi n \tau_l f_0} e^{j2\pi f_{D,l}(qT_s + (n_a-1)T_f)}, \end{aligned} \tag{8}$$

where $q = (n_e - 1)N_d + n_d, 1 \leq n_e \leq N_e, 1 \leq n_d \leq N_d, 1 \leq n \leq N_{sc}, 1 \leq n_a \leq N_a$, $\tilde{y}_{n,n_a,q}$ is the received signal at n th subcarrier, when sensing the angle indexed by (n_a, n_e) . \tilde{z}_n is the noise sample and \tilde{s}_n is the baseband signal for the subcarrier n . While T_s is the symbol duration, $f_0 = 1/T_s$. The number of subcarriers and symbols for coherent processing is determined by $N_{sc} = c_0 T_s / (2\Delta r)$ and $N_d = c_0 / (2f_c \Delta v T_s)$, respectively, where c_0 is the speed of light in free-space, and Δr and Δv denote the range and velocity resolutions, respectively. It is assumed that the communication beam is constant during T_f , the time of one communication packet. At each scanning angle, \mathbf{w}_s and consequently \mathbf{w}_{JCAS} in (6) are calculated, and $\tilde{y}_{n,n_a,q}$ is obtained by (8).

- **Range-Doppler Estimates.** To estimate the range-Doppler of targets, first \tilde{s}_n is removed from the received signal and then the inverse fast Fourier transform (IFFT) and fast Fourier transform (FFT) are applied [23] as:

$$\begin{aligned} \tilde{c}_{n,n_a,q} &= \tilde{y}_{n,n_a,q} / \tilde{s}_n = \tilde{h}_{n,n_a,q} - \tilde{z}_n / \tilde{s}_n, \\ \mathbf{D}_{n_a,n_e} &= \text{FFT}_n [\text{IFFT}_k [\tilde{c}_{n,n_a,q}]] \end{aligned} \tag{9}$$

where $\mathbf{D}_{n_a, n_e} \in \mathbb{C}^{N_d \times N_{sc}}$ is the range-Doppler profile when scanning the angle indexed by (n_a, n_e) .

- **Angular estimates.** The angle estimation is based on beamforming through weighting vector \mathbf{w}_s . As the sensing is in the scanning mode, the Cramér–Rao lower bound (CRLB) for the angle estimation of Δ is [10]:

$$CRLB_{\Delta} \propto \frac{\theta_{3dB}^2}{SNR}, \text{ where } SNR = \frac{\mathbb{E}[|\tilde{h}_{n, n_a, k}|^2]}{\mathbb{E}[|\tilde{z}_n / \tilde{s}_n|^2]}, \tag{10}$$

where θ_{3dB} is the 3 dB-beamwidth of the radiation pattern of the array, which is assumed to be constant for all the angles Δ s in FoV, and SNR is the signal-to-noise ratio defined by (10) according to (9).

2.3.2. JCAS Scenario 2: Overlapping Communication and Sensing Beams When the UE Blocks the Sensing Target

Communication Performance. When the UE blocks the sensing link, the two beams are aligned and superimposed; the whole energy is captured by the UE, then the spectral efficiency is increased. Since $\mathbf{w}_{JCAS} = \sqrt{2}\mathbf{w}_c$, the superimposed channel is $R = \log_2 \det(1 + 2\mathbf{H}^* \mathbf{H} / \sigma_n^2)$. This happens either in the scanning mode of sensing or the tracking mode with the range of the target being larger than the range of UE as in Figure 4b.

Sensing Performance. When the UE blocks the sensing target, the BS can no longer sense/detect the target and the BS has lost the target; on the other side, the target does not cause communication link degradation.

2.3.3. JCAS Scenario 3: Overlapping Communication and Sensing Beams When the Sensing Target Blocks the UE

Let us study the overlapping when the range of the target is smaller than the range of the UE, as in Figure 4c. It is supposed that the human as the target occupies only one angle step, is tracked, and the sensing beam is aligned with the angle of the target. Whether the human is a point or an extended target, depends on the spatial resolutions. The maximum bandwidth of the n261 band of 5G is 400 MHz, which equals 37.5 cm range resolution. Besides, the distance of a human from the BS can be, e.g., 70 m, then in such a distance with a 10° beamwidth of the aperture, the cross-range resolution equals 6.1 m. The assumption in this paper is that a human can fit in a single spatial bin, and is a point target. The mono-static radar-cross-section (RCS) of the human, which also depends on the incident angle, is $[-3.6, -5.2]$ dBsm at 28 GHz [37].

Communication Performance. When an environment object moves into the Fresnel zone of the communication link, the target first serves as the multipath reflector/scatterer and results in multipath interferenced to the LoS signal of the communication link; then the target, depending on its RCS, could totally block the communication link and cause deep fading and thus severe communication link quality degradation. When the target moves towards the communication link, the beams are overlapping, the LoS link vanishes and blockage occurs. In order to model the blockage, the following channel model from BS to the single antenna UE is considered with and without blockage [38,39]:

$$\mathbf{H} = \begin{cases} \mathbf{H}_{LoS} + \mathbf{H}_{NLoS} + \mathbf{H}_{target,1} & \text{if no overlapping beams,} \\ \mathbf{H}_{NLoS} + \mathbf{H}_{target,2} & \text{if beams overlapping,} \end{cases} \tag{11}$$

where:

$$\begin{aligned} \mathbf{H}_{LoS} &= \mathbf{a}_T(\theta_{UE}, \phi_{UE}) g_T(\theta_{UE}, \phi_{UE}) g_R(\theta_{BS}, \phi_{BS}) \frac{\lambda}{4\pi r_{UE}} e^{-j\frac{2\pi}{\lambda} r_{UE}}, \\ \mathbf{H}_{target,s} &= \mathbf{a}_T(\theta_t, \phi_t) g_T(\theta_t, \phi_t) g_R(\theta_r, \phi_r) \frac{\lambda}{4\pi d_t} \Gamma_{t,s} e^{-j\frac{2\pi}{\lambda} d_t}, s \in \{1, 2\}, d_t = r_t + r_r, \end{aligned} \tag{12}$$

where \mathbf{H}_{NLoS} is the same channel (5) as described in Section 2.3.1, $\mathbf{H}_{target,1}$ and $\mathbf{H}_{target,2}$ denote the channel of BS-target-UE before or after the blockage and during the blockage, respectively. g_T and g_R denote the gains of antennas at BS and UE, respectively. (θ_{UE}, ϕ_{UE}) and (θ_{BS}, ϕ_{BS}) are the angles of the UE viewing from BS and BS viewing from UE respectively. (θ_t, ϕ_t) and (θ_r, ϕ_r) denote the angles of the target viewing from BS and target viewing from UE, respectively. r_t and r_r are the distance between the target and the BS, and the target and the UE, respectively. $\Gamma_{t,1}$ which models the reflection and scattering from the human is calculated by [38]:

$$\Gamma_{t,1}(\delta) = \frac{\epsilon_b \sin \delta - \sqrt{\epsilon_b - \cos^2 \delta}}{\epsilon_b \sin \delta + \sqrt{\epsilon_b - \cos^2 \delta}} + \mathcal{CN}(0, \sigma_b^2) \tag{13}$$

where δ is the incident angle on the body, ϵ_b is the complex permittivity of the body and a zero-mean Gaussian random variable with a standard deviation of σ_b models the non-flat body and swinging limbs. Besides, when the human blocks the LoS link, the result is 20 dB attenuation of power at the receiver UE [40], therefore $\Gamma_{t,2}$, which denotes the diffraction coefficient, equals 0.1 at the operation frequency of 28 GHz. We assume that the target moves in a line perpendicular to the LoS path where $\phi_t = \phi_{UE}$ and only the angle θ_t varies, and its Doppler effects on $\mathbf{H}_{target,s}$ are negligible. The channel modeled in (11) is used for calculating the spectral efficiency.

Sensing Performance. As the sensing is in the tracking mode, we adopt the Bayesian CRLB (BCRLB) for the point target tracking. The Fisher Information Matrix (FIM) at the η^{th} epoch can be written as [41]:

$$\mathbf{J}_\eta = \mathbf{J}_\eta^D + \mathbf{J}_\eta^P(\mathbf{J}_{\eta-1}) \tag{14}$$

where \mathbf{J}_η^D is the data information matrix and \mathbf{J}_η^P is the prior information matrix that depends on the $\mathbf{J}_{\eta-1}^D$. The elements of the data FIM, \mathbf{J}_η^D for the delay, Doppler, and angle are related directly to the SNR at each epoch, however, data FIM for the angle is also inversely related to the 3 dB-beamwidth of the JCAS aperture [41]. When the tracked target is at the angle (θ_s, ϕ_s) , according to (8), the radar channel is related to $\mathbf{w}_{JCAS}^T \mathbf{a}_T(\theta_s, \phi_s) \approx 1/\sqrt{2} \mathbf{w}_s^T \mathbf{a}_T(\theta_s, \phi_s)$ in case of no overlapping and orthogonality of beams, and $\mathbf{w}_{JCAS}^T \mathbf{a}_T(\theta_s, \phi_s) \approx \sqrt{2} \mathbf{w}_s^T \mathbf{a}_T(\theta_s, \phi_s)$ when the beams are overlapping, therefore SNR in (10), when beams are overlapping, is four times larger than that of no overlapping. A decrease in BCRLB is expected in the overlapping of beams, and the magnitude of the decrease depends on the prior information as well, which we do not study in detail.

3. Numerical Analysis

3.1. JCAS STPA—A Design Example

Following the JCAS aperture design pipeline in Figure 3, let us start with a uniform array with $A_x \times A_y = 30 \times 30$ elements, with $\lambda/2$ inter-element distance where λ is the wavelength at the center frequency of operation $f_c = 28$ GHz.

First in a global scale, the uniformly and planarly placed antennas are tiled with dominoes based on the maximum entropy, as shown in Figure 5a. In order to show the capability of this large tiled array when scanning to $\theta_{max} = 30^\circ$ according to 5G base station requirements [14], its EBP, which corresponds to the scanning by linear beamforming, is shown in Figure 5b, where the maximum SLL is -13.24 dB and the beamwidth is $r_b = 0.065$.

Second, on a local scale, the sunflower array is used to thin these dominoes. In order to cover the whole aperture, the distance between two neighboring elements of the sunflower array is related to the parameter $s = 3.5\lambda$ (see Appendix A). The domino tiles that are in r_c distance from the elements of the sunflower are chosen for the subarrays, and the thinning rate depends on this r_c . The simulation showed that $r_c = 1.15\lambda$ provides the best performance for low SLL and minimum required tiles, which results in 125 dominoes overall, as shown in Figure 6.

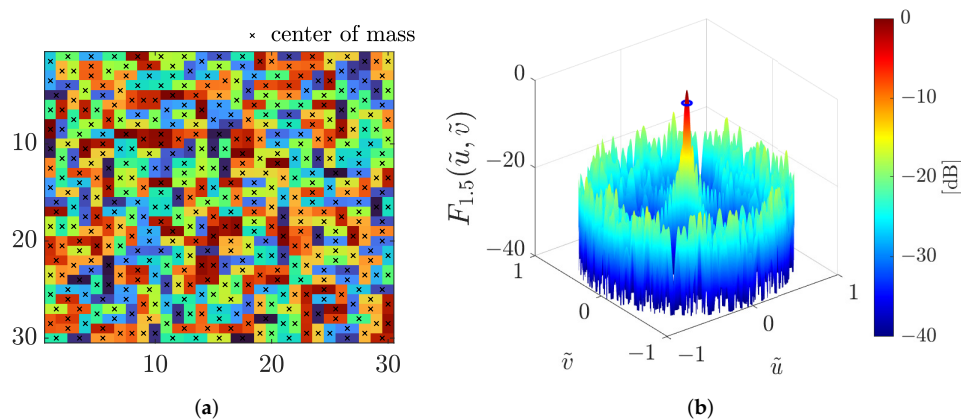


Figure 5. (a) The tiled array with dominoes (the colors are only for differentiating the tiles), (b) its EBP with the blue circle with radius $\tilde{r}_b = 0.043$ denotes the 3 dB-beamwidth of the main beam in (\tilde{u}, \tilde{v}) -space. The beamwidth in (u, v) -space is then $r_b = \zeta\tilde{r}_b = 0.065$.

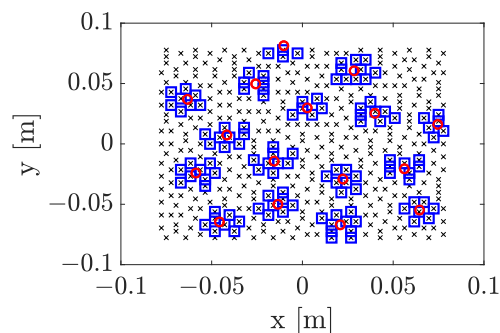


Figure 6. The subarrays chosen based on the sunflower array. The crosses denote the phase centers of the dominoes, the red circles show the centers of the subarrays, and the blue squares demonstrate the chosen dominoes in each subarray.

This elimination of dominoes increases the maximum SLL (reaching -10.93 dB), however, the locations of subarrays can also be optimized for improving the SLL via iterative convex optimization (see Appendix B). The parameters in the position optimization of subarrays for an EBP with $\zeta = 1.5$ are $\tilde{r}_b = 0.043$ for the main beamwidth and $\mu = \lambda/25$ for the maximum of position steps. The angles $0^\circ \leq \theta \leq 90^\circ$ and $-180^\circ \leq \phi < 180^\circ$ are swept with 1° . The objective function is to minimize the maximum SLL in the EBP. As shown in Figure 7a,b, the optimization reaches a maximum SLL of -13.95 dB. For mutual coupling and implementation considerations, the distances of each tile in a subarray to the adjacent tiles in other subarrays are checked to be larger than λ , which is shown in Figure 7c. The EBP of the final geometry has an SLL of -13.5 dB (due to the linear approximation in the optimization) while having a beamwidth of $\tilde{r}_b = 0.043$ as shown in Figure 7d. This final array geometry in Figure 7a will be used for JCAS performance evaluation.

The performance of this proposed STPA is analyzed in various scenarios in comparison to the classical CUPA and SPA. CUPA is a common choice for communication applications, whereas SPA is often utilized in sensing applications. For a fair comparison in regard to antenna element numbers, CUPA is constructed by a rectangular uniform array with 12×12 antennas; 19 antennas at the 4 corners, which are indicated by plus markers in Figure 8a, are removed and 125 antennas remain which construct a uniform planar array that is almost symmetric in x and y axes as in Figure 8a. Figure 8d shows the EBP of this CUPA with a maximum SLL of -15.6 dB. The SPA design is based on the pattern of a sunflower array [42] with 125 antennas. Note that a maximum SLL for such SPA can even be -16.75 dB when its aperture radius equals 3.7λ . However, we require the same aperture radius and beamwidth as that for STPA, therefore we apply an aperture radius of 6.8λ as in

Figure 8b, and the resultant maximum SLL is -10.59 dB as in Figure 8e, which is higher than maximum SLL of STPA -13.41 dB as in Figure 8f.

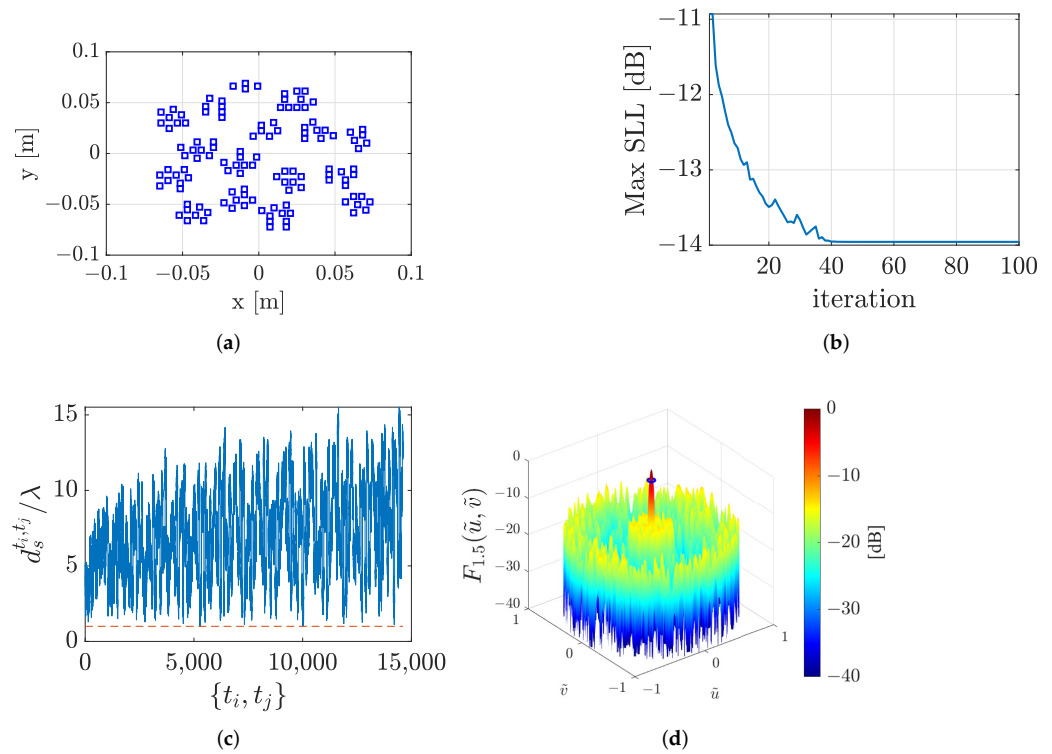


Figure 7. (a) The final geometry of subarrays where the blue squares are the centers of domino tiles, (b) maximum SLL during iterative optimization on the position of subarrays, (c) $d_s^{t_i, t_j}$, the distance of tiles t_i and t_j when they are not in the same subarray and the x -axis is the enumeration of $\{t_i, t_j\}$ pairs and (d) the EBP of aperture with the blue circle on the main beam indicating the 3 dB-beamwidth.

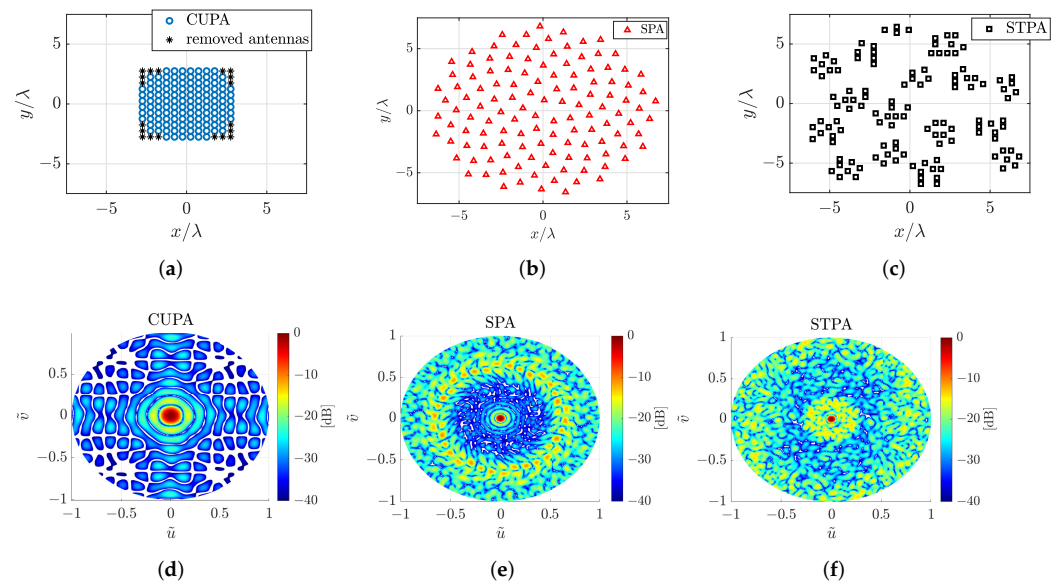


Figure 8. The elements configurations for (a) CUPA, (b) SPA and (c) STPA. The EBP with $\zeta = 1.5$ for (d) CUPA, (e) SPA and (f) STPA.

3.1.1. Robustness of STPA to Wideband Operation

The EBPs in Figure 8d–f are obtained at the center frequency f_c , however, these apertures will be employed in wideband JCAS. Therefore, a study on the SLLs of EBPs versus a change in the operating frequency is required. The decrease from f_c is not problematic on the SLLs since the wavelength is increased and the distance between elements is already enough for radiation with low SLLs. Then, the increase of operating frequency from f_c is studied. Figure 9 demonstrates how these designed apertures perform with an increase in the frequency of operation. We observe that the EBP of STPA at $f/f_c = 1.625$ still shows a maximum SLL of -11.41 dB, but the CUPA suffers from high SLL (grating lobes). The maximum frequencies for CUPA and STPA are $1.125 f_c$ and $1.625 f_c$, respectively. Due to a higher irregularity of the SPA and its sufficient inter-distances of antennas, the maximum SLL for SPA does not vary much. SPA demonstrates a maximum SLL of -10.59 dB that is constant over the considered bandwidth.

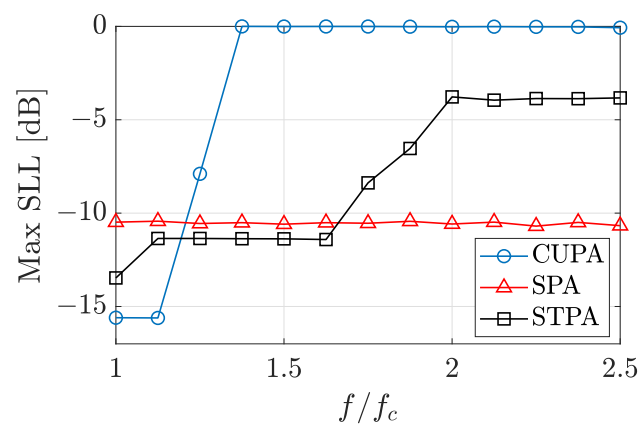


Figure 9. The level of maximum SLL in EBP with $\zeta = 1.5$ for CUPA, SPA and STPA.

3.1.2. Practical STPA Design

An example of an STPA is simulated in CST Studio. The radiating elements are patch antennas, as in Figure 10a, designed on the Rogers RO3003 substrate with a thickness of 0.25 mm, a relative permittivity of $\epsilon_r = 3$, a copper cladding thickness of 35 μm , and excited by discrete ports. At $f_c = 28$ GHz, the 10 dB-bandwidth is 863 MHz and the 3 dB-beamwidth is $\theta_{3dB} < 29.1^\circ$ for various ϕ s. Upon the knowledge of the positions of phase centers for tiles, as shown in Figure 7a and the orientation of dominoes (horizontal or vertical), the STPA has obtained and shown in Figure 10b. The radiation from the STPA can be simulated by simultaneous excitation of the two horizontally or vertically juxtaposed patch antennas (corresponding to a tile) with the same phase. The number of patch antennas is 250, whereas the number of phase shifters and tiles is 125. As an example, the S11 parameters of 18 antennas (9 dominoes) at subarray 1 are shown in Figure 10c when all antennas are excited simultaneously for scanning $(\theta, \phi) = (0^\circ, 0^\circ)$ and Figure 10d for scanning $(\theta, \phi) = (30^\circ, 45^\circ)$. The changes in the resonance frequency and magnitude of S11 are noticeable due to the mutual coupling effects. The radiation from the STPA at the frequency of 28 GHz and beamformed to boresight $(\theta, \phi) = (0^\circ, 0^\circ)$ is shown in Figure 10e where the maximum directivity is 29.4 dB, the 3 dB-beamwidth is 8° , and the maximum SLL is -13.6 dB, whereas in case of beamformed towards $(\theta, \phi) = (30^\circ, 45^\circ)$, the maximum directivity is 26.5 dB, the maximum SLL reaches -11.9 dB and 3 dB-beamwidth to 9.2° , as shown in Figure 10f. The decrease of directivity and SLL suppression in the full-wave simulations is due to the non-isotropic radiation of patch antennas, the mutual coupling effects, and the asymmetric radiations of horizontal and vertical tiles.

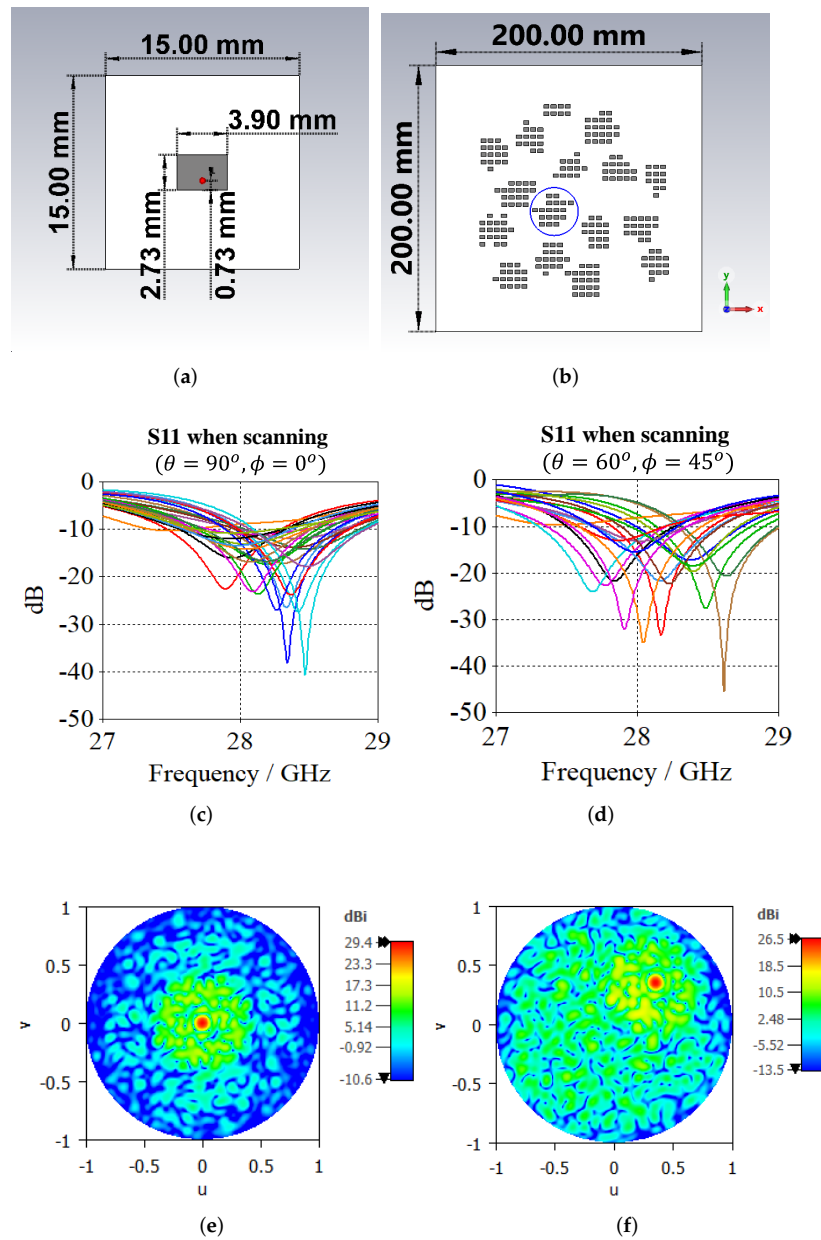


Figure 10. (a) The geometry of the patch antenna element in CST, with the red dot denoting the feeding point (b) the arrays of antennas and the blue circle denoting subarray 1, (c) S11-parameters of 18 antennas at subarray 1 when scanning ($\theta = 0^\circ, \phi = 0^\circ$), (d) S11-parameters of 18 antennas at subarray 1 when scanning ($\theta = 30^\circ, \phi = 45^\circ$) (e) the radiation pattern of the array when scanning ($\theta = 0^\circ, \phi = 0^\circ$) (f) the radiation pattern of the array when scanning ($\theta = 30^\circ, \phi = 45^\circ$).

3.2. STPA Performances in JCAS Scenarios and Benchmarking

Above, we have demonstrated the practicality of implementing STPA by using full-wave simulation (hence feasible for fabrication). We now proceed with communication and sensing scenarios and performances. In order to focus on the array configuration and for the sake of the simulation consistency, we use the analytical model of the STPA with isotropic radiating elements (instead of the CST full-wave model) for analyzing the JCAS performance in comparison with CUPA and SPA.

3.2.1. Communication Performance in Scenario 1: Non-Overlapping Communication and Sensing Beams

We consider the situation in Figure 4a and assume a UE with a single-isotropic antenna in the range of $r_{UE} = 50$ m and an angle of $(\theta_{UE}, \phi_{UE}) = (20^\circ, 50^\circ)$. The channel in (5) from the JCAS aperture to the user is modeled by a dominant LoS path, besides NLoS paths, which include $N_{cl} = 8$ clusters each with $N_{ray} = 10$ rays and having 10 dB power less than the LoS path. The overall power of the channel, including LoS and NLoS paths, is normalized for the channel, as in [14]. The scatters are distributed uniformly within all elevations $0^\circ \leq \theta \leq 90^\circ$ and azimuth $-180^\circ \leq \phi < 180^\circ$ angles. The channel from BS to the user via the target $\mathbf{H}_{target,1}$ is also considered in the NLoS path. Based on the estimated channel and desired scanning angles, \mathbf{w}_{JCAS} and based on that, the spectral efficiency R can be calculated. The average of R from 200 channel realizations is obtained, where the scatters at random angles are generated at each realization. As shown in Figure 11, all apertures demonstrate the same spectral efficiency for the LoS communication, since the gains of the three apertures at the direction of the UE are equal. However, the advantages of STPA are its modular design compared to SPA and the superiority of its sensing capabilities over CUPA, which is studied in the following section.

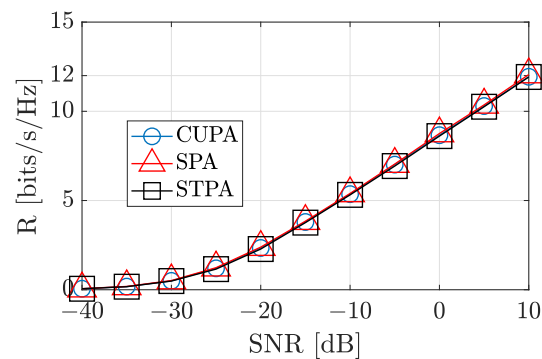


Figure 11. The spectral efficiency for the designed CUPA, SPA, and STPA when there is no overlapping of communication and sensing beams. SNR denotes the SNR level in the LoS path.

3.2.2. Sensing Performance in Scenario 1: Non-Overlapping Communication and Sensing Beams

One of the key performance metrics for sensing is the angular resolution in the scanning mode, which is studied here for the STPA in comparison to CUPA and SPA. STPA and SPA have a smaller beamwidth than CUPA and presumably perform better at target detection [10]. Besides, the quality of SLLs is different for STPA and SPA, which influences the detection results. We adopt a Monte Carlo simulation to study these effects. The scenario in Figure 4a is considered, where UE and the targets are distributed in the FoV of JCAS apertures. Suppose that UE is located in the same range and angle as before and the targets are in a square region at z -axis, and generate N_{targets} point targets at $z_{\text{targets}} = 70$ m, as shown in Figure 12. The targets have the same velocities of $v_{\text{targets}} = 20$ m/s and their x and y coordinates are sampled uniformly from $x \in [x_{\min}, x_{\max}]$ and $y \in [y_{\min}, y_{\max}]$ where $x_{\max} = -x_{\min} = y_{\max} = -y_{\min} = z_{\text{targets}} \times \tan \theta_{\max}$. Note that if a target coincides with the angle of UE, it is neglected. Suppose $\mathbf{A}^p = [a_1^p, \dots, a_{N_{\text{targets}}}^p]$ is a matrix containing the Cartesian coordinates of p^{th} set of targets, where $a_{n_t}^p = (x_{n_t}^p, y_{n_t}^p)$ for n_t^{th} target. The radiation gain of JCAS tiles and auxiliary antennas, and the noise figure of the receiver, are assumed to be unit. Then, the two-way channel gain in (5) is $b_l = \frac{\lambda^2}{(4\pi)^3 r_l^2}$, where r_l is the range of l^{th} target. The carrier frequency is $f_c = 28$ GHz and the symbol duration equals $T_s = 51.2 \mu\text{s}$. The coherent processing duration for Doppler estimation is $N_d T_s$ and a communication packet includes $N_d N_e$ symbols. Here, we intend to compare these apertures in the worst scenario, namely all targets are located at the same range and velocity bins but different cross-range bins. Therefore, to expedite the Monte Carlo simulations,

simply $N_{sc} = 8$ and $N_d = 8$. The spatial sampling is adjustable according to the purpose of scanning, here $N_x = N_y = 60$ provides sufficient resolutions, where N_x and N_y are the numbers of bins in the x -axis and y -axis, respectively. We applied a conversion from Cartesian to spherical coordinate on the points in FoV and then utilized (8) to generate synthetic data, and then employed (9) for range-Doppler and angle estimation of targets. The images in x - y plane are generated, and cell averaging 2D constant false alarm rate (CA-CFAR) detection is applied with a guard band size of [2,2] and a training band size of [5,5]. As CA-CFAR determines its threshold based on a measured SNR in training cells to guarantee a constant probability of false-alarm P_{FA} , a variation of SNR in simulations is therefore pointless. Instead, we study a variation in $P_{FA} = \{10^{-3}, 10^{-2}, 10^{-1}\}$. Depending on the level of threshold resulting from different P_{FA} s, the number of detection points can vary. The density-based spatial clustering of applications with noise (DBSCAN) is applied to cluster the detected points, where a threshold for a neighborhood search radius of 0.05 and a minimum number of neighbors of 1 are considered. Then the number of clusters is the number of detected targets $N_{\text{targets}}^{\text{detected}}$ and the centroid of each cluster is supposed to be the coordinate of the detected target. The association of the estimated and true targets is based on the k -nearest neighbors (k -NN) algorithm, where a single nearest neighbor to a true target is determined by the Minkowski distance of second.

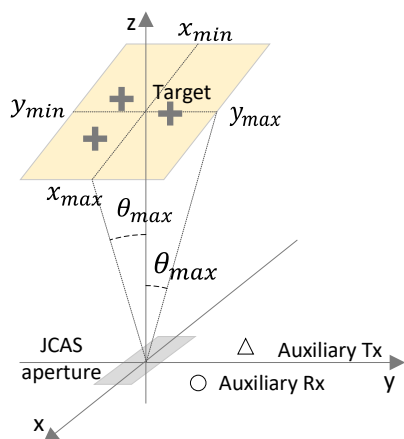


Figure 12. The investigation domain in FoV for scenario 1.

Before introducing the quantitative metrics for comparison of sensing by these apertures, an example of a sensing scenario is provided here. The detection of 8 randomly generated targets at $SNR = 10$ dB and $P_{FA} = 10^{-2}$ are simulated. The normalized images and qualitative performance are shown in Figure 13a,b for CUPA, where only 5 targets are detected and 3 are missed. In Figure 13c,d for SPA, 7 targets are estimated and 1 target is missed. Finally, in Figure 13e,f for STPA, 6 targets are estimated and 2 are missed.

Therefore, we adopt two quantitative performance metrics; namely *detection loss rate* (DLR) and *root-mean-square error* (RMSE). Due to different beamwidths, the maximum detectable targets $N_{\text{targets}}^{\text{max}}$ for these apertures are different, and considering a symmetrical FoV of $2\theta_{\text{max}}$ in x and y axes as in Figure 12b, it is obtained by $N_{\text{targets}}^{\text{max}} = \lfloor (2\theta_{\text{max}})/(\theta_{3\text{dB}}/2) \rfloor^2$. Considering the radiation patterns in Figure 8d–f, the 3 dB-beamwidths $\theta_{3\text{dB}}$ for CUPA, SPA, and STPA are 24° , 10° and 10° , respectively, therefore $N_{\text{targets}}^{\text{max,CUPA}} = 25$ and $N_{\text{targets}}^{\text{max,SPA}} = N_{\text{targets}}^{\text{max,STPA}} = 144$. Knowing $0 < N_{\text{targets}}^{\text{detected},p} < N_{\text{targets}}^{\text{max}}$ for p^{th} set of targets, we define a normalized detection (ND) as $ND^p = N_{\text{targets}}^{\text{detected},p} / N_{\text{targets}}^{\text{max}}$ which, as a random variable, follows a Beta distribution with an average value of μ_{ND} . DLR basically accounts for the discrepancy in the number of detected $N_{\text{targets}}^{\text{detected}}$ and true targets N_{targets} , and is defined as:

$$DLR = \frac{|\mu_{ND} N_{\text{targets}}^{\text{max}} - N_{\text{targets}}|}{|N_{\text{targets}}^{\text{max}} - N_{\text{targets}}|} \tag{15}$$

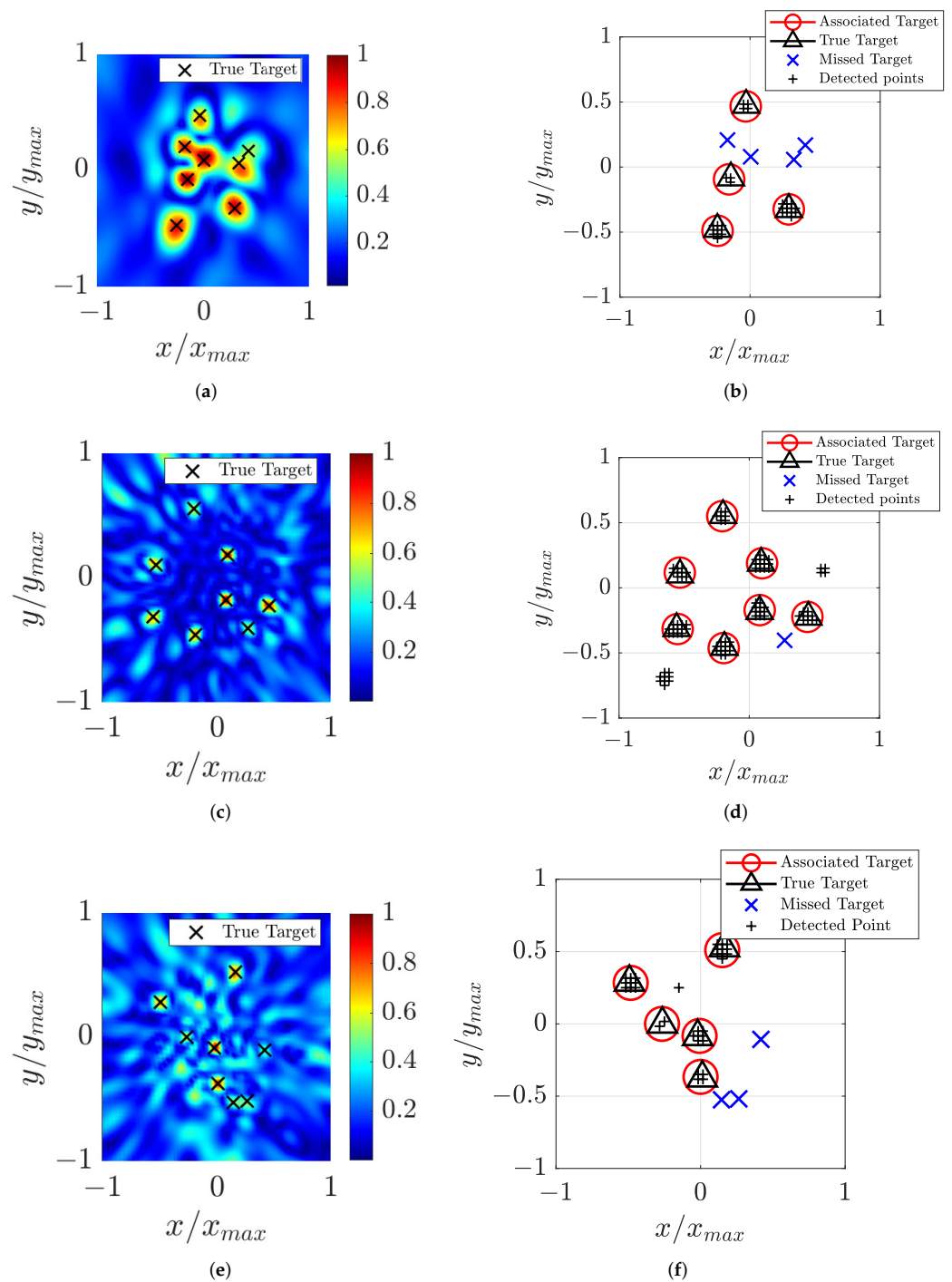


Figure 13. Normalized images, associated, missed, and true targets for (a,b) CUPA, (c,d) SPA, and (e,f) STPA.

Ideally, DLR equals zero, however, it is often a positive number, particularly when N_{targets} increases or the angular resolution of the aperture is limited, therefore $0 < DLR < 1$, and it is the first metric for comparison. The RMSE of true and estimated targets is defined as:

$$RMSE(\hat{\mathbf{A}}^p, \mathbf{A}^p) = \sqrt{\frac{1}{N_{\text{targets}}} \sum_{n_i=1}^{N_{\text{targets}}} |\hat{a}_{n_i}^p - a_{n_i}^p|^2} \quad (16)$$

where $\hat{\mathbf{A}}^p$ denotes the estimated coordinates of p^{th} set of targets. The RMSE as a random variable can be modeled by Rayleigh distribution, with an average value of μ_{RMSE} , which is the second metric to compare the performance of these apertures. The process of generating targets and calculating DLR and RMSE is repeated for $P = 200$ times at $SNR = 10$ dB. DLR and μ_{RMSE} are calculated for these apertures in $P_{FA} = \{10^{-3}, 10^{-2}, 10^{-1}\}$ and $N_{\text{targets}} = \{4, 8, 12\}$. Figure 14a–c demonstrate that DLR for CUPA is larger than SPA and STPA in any P_{FA} and N_{targets} . STPA also has higher DLR than SPA. The effect of the increase in N_{targets} can be observed in all apertures where DLR increases accordingly. The increase in P_{FA} results in the decrease in DLR for all apertures.

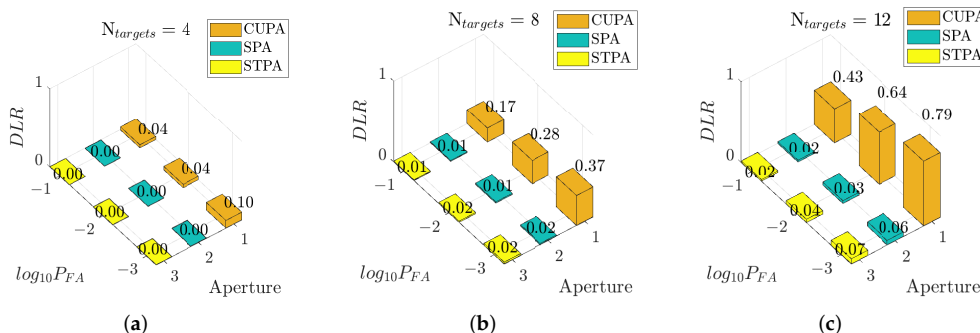


Figure 14. The DLR when (a) $N_{\text{targets}} = 4$, (b) $N_{\text{targets}} = 8$ and (c) $N_{\text{targets}} = 12$.

Figure 15a–c shows the μ_{RMSE} for these apertures, where the performances, although similar, are still comparable, as in $\mu_{RMSE}^{\text{CUPA}} > \mu_{RMSE}^{\text{STPA}} > \mu_{RMSE}^{\text{SPA}}$ for all P_{FA} s and N_{targets} s. Although the angular resolutions of SPA and STPA are smaller than CUPA, the differences in μ_{RMSE} are small due to the possible side lobes, which can create ghost targets and result in errors in the location of targets. By observing the EBP of SPA and STPA in Figure 9e,f, the SLLs in the neighborhood of the main beam at $(\tilde{u}, \tilde{v}) = (0, 0)$ in STPA are higher than that of SPA, which causes more errors in the accurate detection and association of targets, therefore $\mu_{RMSE}^{\text{STPA}} > \mu_{RMSE}^{\text{SPA}}$.

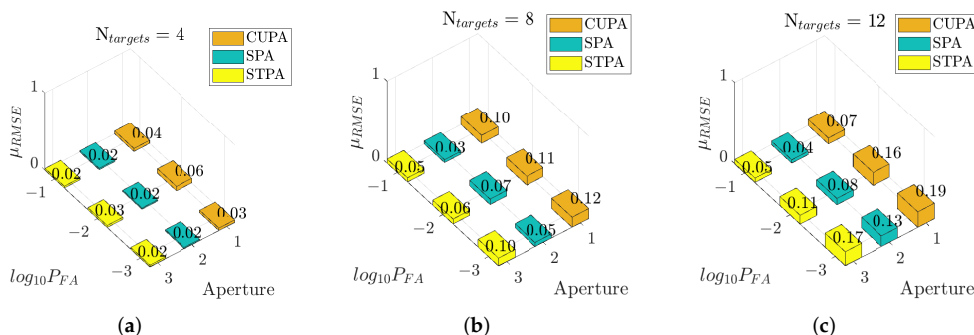


Figure 15. The average of RMSE when (a) $N_{\text{targets}} = 4$, (b) $N_{\text{targets}} = 8$ and (c) $N_{\text{targets}} = 12$.

3.2.3. Communication Performance in Scenario 2: Overlapping Communication and Sensing Beams When UE Blocks the Sensing Target

As the same waveform is used for both beams, when overlapping occurs either in the scanning mode or in the tracking mode with the range of the tracking target being larger than the range of the UE, which is the case in Figure 4b, the signal power at the UE is increased, therefore spectral efficiency is supposed to increase. Let us consider that if the user is at the angle $(\theta_{UE}, \phi_{UE}) = (20^\circ, 50^\circ)$, the sensing is in the scanning mode and the sensing beam first scans over azimuth at the elevation $\theta = 20^\circ$ and then over elevation at azimuth $\phi = 50^\circ$ angles. The average spectral efficiencies at an SNR of 10 dB are presented in Figure 16a,b. The deviation from the spectral efficiency without overlapping is noticeable for the STPA only when the difference between the communication angle and scanning

angle is 10° , whereas this number for the CUPA is 24° . STPA and SPA perform similarly in this case. Figure 16a,b and the discussion above on the communication link are also valid for the tracking mode of a target with a larger range than the UE, e.g., $r_{UE} = 70$ m and $r_t = 140$ m, since the tracking and communication beams are overlapping and the power in the resultant aggregated beam is captured by the UE. Regarding sensing performance in these cases, the received signal at the BS from the scanning or tracking beam when it reaches the angle of the UE is negligible due to weak reflection from UE, which is the assumption in this paper. In the overlapping when the tracked target is behind the UE, the received reflected signal at the BS is zero again and the target is also lost. The spectral efficiency of the communication link increased since the sensing and communication beam have the same waveform, if one intends to use separate waveforms in separate beams, then beam overlapping is detrimental for the SNR at the user.

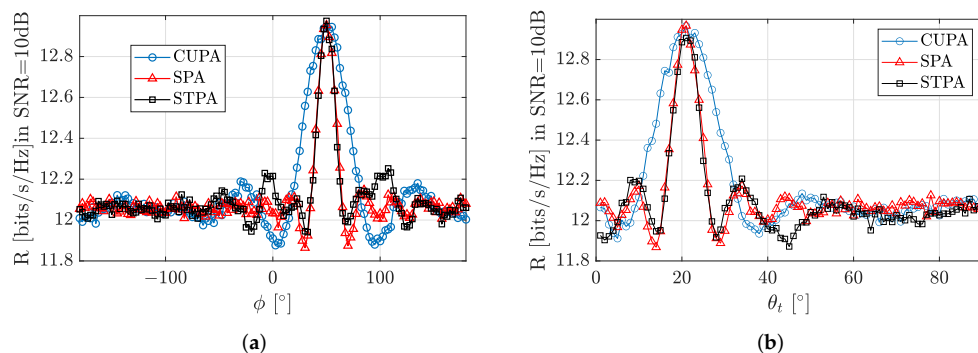


Figure 16. The effect of the scanning beam on the spectral efficiency for the STPA compared with CUPA and SPA while scanning in (a) azimuth, and (b) elevation.

3.2.4. Communication Performance in Scenario 3: Overlapping Communication and Sensing Beams When the Sensing Target Blocks the UE

The range for UE is considered to be $r_{UE} = 70$ m, the target body moves at the constant azimuth of $\phi_t = 50^\circ$, perpendicular to the LoS path, crossing it at $r_m = 35$ m, as in Figure 4c. The parameters for the body in (13) are assumed as $\epsilon_b = 0.1 - j2.33$, $\sigma_b = 0.45$ dB [38] and the incident angle on the body $\delta = \theta_t$. The variation of spectral efficiency at an SNR of 10 dB for the STPA, CUPA, and SPA are shown in Figure 17. There is an increased oscillation in the spectral efficiency just before and after blockage occurrence, which is due to the constructive and destructive addition of $\mathbf{H}_{target,1}$ and \mathbf{H}_{LoS} [43]. The most noticeable difference between the STPA and CUPA is the time of blockage where the STPA, due to its narrower beamwidth, has a shorter blockage time. In these scenarios, the blockage time is proportional to the overlapping angles of communication and sensing beam, hence it is observed in Figure 17 that the STPA has a 40% shorter blockage time than CUPA in the scanning of the elevation angle. The blockage time and oscillation of STPA and SPA are not noticeably different.

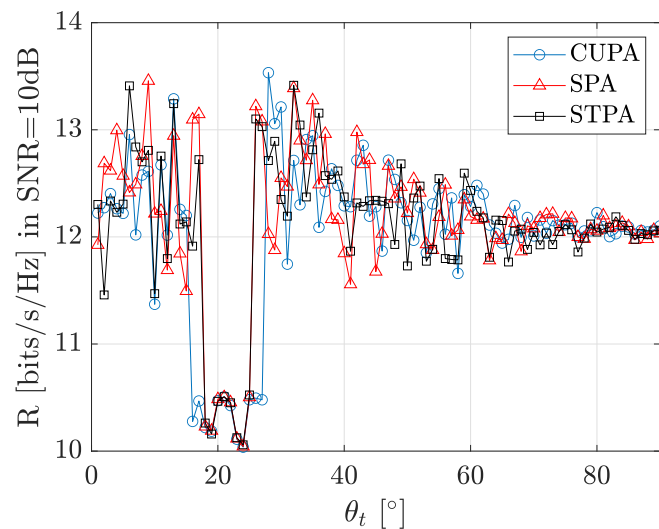


Figure 17. The spectral efficiency when the target blocks the LOS path at the angle $\theta_t = 20^\circ$.

3.3. Findings from Benchmarking

In this paper, we assumed a scenario with a dominant LoS path, therefore the increase in the average SLL due to tiling and sparse design of STPA and SPA was not detrimental to communication performance, as all apertures demonstrated the same spectral efficiency. The sensing performance of STPA is between CUPA and SPA. The effect of smaller beamwidth of STPA and SPA is reflected in a smaller DLR than the one of CUPA. However, the higher SLLs of SPA and STPA can still result in errors in detection, which results in similar RMSE for these three apertures. The results demonstrate that the SPA has slightly smaller DLR and RMSE than the ones of STPA. This was expected as SPA has a lower average SLL than STPA due to the freedom in the location of its elements, but this freedom makes the manufacturing of SPA more complex. STPA is uniformly distributed in the subarray level and easier to manufacture, although it still has a sparse subarray structure.

4. Conclusions

Analog beamforming arrays can increase the gain of radiation and overcome propagation attenuation in millimeter wave communication and sensing links. Therefore, in alliance with the fully-connected analog beamforming arrays, a sparse tiled planar array (STPA) is proposed for joint communication and sensing (JCAS) applications. The benchmarks are a conventional uniform planar array (CUPA) and a sparse planar array (SPA).

- *The array configuration* of STPA is based on a modular design, narrow beamwidth, and decreased number of phase shifters. The design is based on maximum entropy in the phase centers of the tiles in the array and sparse subarrays. The results show that an STPA with 125 domino tiles has stable radiation up to 1.625 times the center frequency of operation, whereas this number is 1.125 for CUPA. A realistic radiation pattern of an STPA, including antenna imperfections, is shown by full-wave simulation.
- The results show improvement in *sensing performance*, namely, when the sensing and communication beams are not overlapping, CUPA, SPA, and STPA guarantee the same spectral efficiency in the communication link, whereas a better angular resolution is achieved by SPA and STPA in sensing, e.g., the simulations show that the detection loss rate for STPA and SPA are less than for CUPA. The side lobes in SPA and STPA also result in the same average error in detection as CUPA. The percentages of improvement in detection loss and accuracy depend on the number of targets and false-alarm probability, which were the parameters of study.
- *JCAS performance* is analyzed through blockage time when the sensing beam is tracking a target and overlapping with the communication beam. As SPA and STPA have a

narrower beamwidth than the CUPA, the blockage time is 40% shorter while the target moves towards the boresight of the apertures. Finally, we conclude that STPA can be utilized when a smaller beamwidth with a modular design is desired, otherwise SPA still outperforms STPA in sensing performance.

In future works, there is space to further improve the aperture efficiency of the designed STPA. This can be tackled by assigning tiles with different sizes to the outer sub-arrays. Regarding communication, the effect of SLLs of SPA and STPA on the NLoS and multi-users communication case is still an open question. Regarding sensing, the tracking of extended or multiple targets demands a dynamic pattern configuration in which narrow beamwidth or high SLL may not be optimum. Therefore, beam squinting or antenna selections can also be applied then.

Author Contributions: Conceptualization, H.A., A.K. and Y.M.; Methodology, H.A. and Y.M.; Software, H.A.; Validation, H.A., A.K. and Y.M.; Formal analysis, H.A. and Y.M.; Investigation, H.A.; Writing—original draft, H.A. and Y.M.; Writing—review & editing, A.K.; Supervision, A.K. and Y.M.; Project administration, Y.M.; Funding acquisition, Y.M. All authors have read and agreed to the published version of the manuscript.

Funding: This research was funded by the Dutch Sector Plan.

Data Availability Statement: The data presented in this study are available on request from the corresponding author.

Conflicts of Interest: The authors declare no conflict of interest.

Appendix A. Sunflower Array

The sunflower array can demonstrate the same radiation pattern as a uniform array, but with a lower number of antennas. In polar coordinates, the m th element of the sunflower array (ρ_m, ψ_m) is obtained by [15]:

$$\rho_m = s\sqrt{\frac{m}{\pi}}, \psi_m = 2\pi m\tau \text{ where } m = 1, 2, \dots, M \quad (\text{A1})$$

where s is the parameter relating the distance of two neighbor elements, τ denotes the angular displacement of two consecutive elements, which equals 1.618 the golden ratio, and M is the number of elements.

Appendix B. Position Optimization

The positions of subarrays are optimized based on an iterative convex optimization. Let us consider the expanded radiation field of the array in (\tilde{u}, \tilde{v}) -space as:

$$f_{\zeta}^i(\tilde{u}, \tilde{v}) = \frac{1}{N} \sum_{n=1}^N e^{jk_{\zeta}(\tilde{u}x_n + \tilde{v}y_n)}, \quad (\text{A2})$$

As it is discussed in Ref. [44], when the positions of antennas are optimization variables, the problem is nonlinear and non-convex, however it can be solved as a convex problem iteratively by first-order Taylor expansion, as in:

$$\begin{aligned} f_{\zeta}^i(\tilde{u}, \tilde{v}) &= \frac{1}{N} \sum_{n=1}^N e^{jk_{\zeta}\tilde{u}x_n^{i-1}} (1 + jk_{\zeta}\tilde{u}\epsilon_n^i) e^{jk_{\zeta}\tilde{v}y_n^{i-1}} (1 + jk_{\zeta}\tilde{v}\beta_n^i) \\ &\approx \frac{1}{N} \sum_{n=1}^N e^{jk_{\zeta}\tilde{u}x_n^{i-1}} e^{jk_{\zeta}\tilde{v}y_n^{i-1}} (1 + jk_{\zeta}\tilde{u}\epsilon_n^i + jk_{\zeta}\tilde{v}\beta_n^i), \end{aligned} \quad (\text{A3})$$

where $|\beta_n^i| \ll 1, |\epsilon_n^i| \ll 1$

where i denotes the iteration index, and e_n^i and β^i are the movement in x and y axes at i th iteration, respectively. x_n^{i-1} and y^{i-1} are the position in x and y axes at $(i-1)$ th iteration, respectively. (A3) is a linear convex function that can be solved by Matlab CVX [45]. To enforce only subarray movements, $\{e_n^i, \beta_n^i\}$ s are equal for all antennas in a subarray. Finally, the optimization can be written as:

$$\begin{aligned} \min_{E^i, B^i} \quad & \gamma^i \\ \text{s.t.} \quad & \max(|f_{\zeta}^i(\{\tilde{\mathbf{u}}, \tilde{\mathbf{v}}\}_{\text{SL}})|) \leq \gamma^i, \\ & \text{real}(f_{\zeta}^i(0, 0)) = 1, \\ & |e_n^i| \leq \mu, |\beta_n^i| \leq \mu, \quad \forall n \in \{1, 2, \dots, N\} \end{aligned} \quad (\text{A4})$$

where $E^i = \{e_1^i, e_2^i, \dots, e_N^i\}$ and $B^i = \{\beta_1^i, \beta_2^i, \dots, \beta_N^i\}$. $\{\tilde{\mathbf{u}}, \tilde{\mathbf{v}}\}_{\text{SL}}$ is the set of all side lobe angles $(\tilde{u}, \tilde{v})_{\text{SL}}$ and μ is a predetermined number. As the elements are domino tiles, there should be a distance of at least λ between the phase center of each domino at one subarray with the phase centers of other dominoes at adjacent subarrays for fabrication possibility. This could also be added as a constraint to (A4), as discussed in Ref. [44].

References

- De Lima, C.; Belot, D.; Berkvens, R.; Bourdoux, A.; Dardari, D.; Guillaud, M.; Isomursu, M.; Lohan, E.S.; Miao, Y.; Barreto, A.N.; et al. Convergent communication, sensing and localization in 6G systems: An overview of technologies, opportunities and challenges. *IEEE Access* **2021**, *9*, 26902–26925. [CrossRef]
- Alidoustaghdam, H.; Miao, Y.; Kokkeler, A. Integrating TDD Communication and Radar Sensing in Co-Located Planar Array: A Genetic Algorithm Enabled Aperture Design. In Proceedings of the 2022 2nd IEEE International Symposium on Joint Communications & Sensing (JC&S), Seefeld, Austria, 9–10 March 2022; pp. 1–6. [CrossRef]
- Alidoustaghdam, H.; Miao, Y.; Kokkeler, A. Widely Linear Beamforming for Full-Duplex Joint Communications and Sensing: An Investigation on Virtual Displacement of Array Elements during Local Optimization. In Proceedings of the 2022 16th European Conference on Antennas and Propagation (EuCAP), Madrid, Spain, 27 March–1 April 2022; pp. 1–5. [CrossRef]
- Zhang, J.A.; Liu, F.; Masouros, C.; Heath, R.W.; Feng, Z.; Zheng, L.; Petropulu, A. An overview of signal processing techniques for joint communication and radar sensing. *IEEE J. Sel. Top. Signal Process.* **2021**, *15*, 1295–1315. [CrossRef]
- Xue, Q.; Liu, Y.J.; Sun, Y.; Wang, J.; Yan, L.; Feng, G.; Ma, S. Beam management in ultra-dense mmwave network via federated reinforcement learning: An intelligent and secure approach. *IEEE Trans. Cogn. Commun. Netw.* **2022**, *9*, 185–197. [CrossRef]
- Oliveri, G.; Gottardi, G.; Massa, A. A new meta-paradigm for the synthesis of antenna arrays for future wireless communications. *IEEE Trans. Antennas Propag.* **2019**, *67*, 3774–3788. [CrossRef]
- Ma, Y.; Yang, F.; Chen, K.; Yang, S.; Chen, Y.; Qu, S.W.; Hu, J. An Irregular Tiled Array Technique for Massive MIMO Systems. *IEEE Trans. Wirel. Commun.* **2021**, *21*, 4509–4521. [CrossRef]
- Athley, F.; Engdahl, C.; Sunnergren, P. On radar detection and direction finding using sparse arrays. *IEEE Trans. Aerosp. Electron. Syst.* **2007**, *43*, 1319–1333. [CrossRef]
- Meng, X.; Liu, F.; Masouros, C.; Yuan, W.; Zhang, Q.; Feng, Z. Vehicular Connectivity on Complex Trajectories: Roadway-Geometry Aware ISAC Beam-tracking. *IEEE Trans. Wirel. Commun.* **2023**, *1*. [CrossRef]
- Gupta, A.; Madhoo, U.; Arbabian, A.; Sadri, A. Design of large effective apertures for millimeter wave systems using a sparse array of subarrays. *IEEE Trans. Signal Process.* **2019**, *67*, 6483–6497. [CrossRef]
- Ma, Y.; Yang, S.; Chen, Y.; Qu, S.W.; Hu, J. Pattern synthesis of 4-D irregular antenna arrays based on maximum-entropy model. *IEEE Trans. Antennas Propag.* **2019**, *67*, 3048–3057. [CrossRef]
- Anselmi, N.; Rocca, P.; Salucci, M.; Massa, A. Irregular phased array tiling by means of analytic schemata-driven optimization. *IEEE Trans. Antennas Propag.* **2017**, *65*, 4495–4510. [CrossRef]
- Dong, W.; Xu, Z.H.; Li, X.X.; Xiao, S.P. Low-cost subarrayed sensor array design strategy for IoT and future 6G applications. *IEEE Internet Things J.* **2020**, *7*, 4816–4826. [CrossRef]
- Ma, Y.; Yang, F.; Huang, M.; Sun, C.; Chen, Y.; Qu, S.W.; Yang, S. A Thinned Irregular Array Synthesis Approach Based on Benders Decomposition. *IEEE Trans. Antennas Propag.* **2020**, *69*, 3875–3885. [CrossRef]
- Viganó, M.C. Sunflower Array Antenna for Multi-Beam Satellite Applications. 2011; pp. 71–79. Available online: <https://repository.tudelft.nl/islandora/object/uuid%3A33e95433-514f-4367-8385-ae3cc9ddc6f5> (accessed on 11 July 2023).
- Anjos, E.V.; SalarRahimi, M.; Bressner, T.A.; Takhiani, P.; Lahuerta-Lavieja, A.; Elsakka, A.; Siebenga, J.S.; Volski, V.; Fager, C.; Schreurs, D.; et al. FORMAT: A reconfigurable tile-based antenna array system for 5G and 6G millimeter-wave testbeds. *IEEE Syst. J.* **2022**, *16*, 4489–4500. [CrossRef]
- Shen, K.; Safapourhajari, S.; De Pessemier, T.; Martens, L.; Joseph, W.; Miao, Y. Optimizing the Focusing Performance of Non-Ideal Cell-Free mMIMO Using Genetic Algorithm for Indoor Scenario. *IEEE Trans. Wirel. Commun.* **2022**, *21*, 8832–8845. [CrossRef]

18. Shen, K.; De Pessemier, T.; Martens, L.; Joseph, W.; Miao, Y. Genetic Algorithm Combined with Ray Tracer for Optimizing Cell-Free mMIMO Topology in a Confined Environment. In Proceedings of the 2021 15th European Conference on Antennas and Propagation (EuCAP), Dusseldorf, Germany, 22–26 March 2021; pp. 1–5. [\[CrossRef\]](#)
19. Aslan, Y.; Puskely, J.; Roederer, A.; Yarovoy, A. Synthesis of quasi-modular circularly polarized 5G base station antenna arrays based on irregular clustering and sequential rotation. *Microw. Opt. Technol. Lett.* **2021**, *63*, 1278–1285. [\[CrossRef\]](#)
20. Aslan, Y.; Roederer, A.; Yarovoy, A. System advantages of using large-scale aperiodic array topologies in future mm-wave 5G/6G base stations: An interdisciplinary look. *IEEE Syst. J.* **2021**, *16*, 1239–1248. [\[CrossRef\]](#)
21. Lin, Z.; Lin, M.; Champagne, B.; Zhu, W.P.; Al-Dhahir, N. Secrecy-energy efficient hybrid beamforming for satellite-terrestrial integrated networks. *IEEE Trans. Commun.* **2021**, *69*, 6345–6360. [\[CrossRef\]](#)
22. Vigano, M.; Toso, G.; Caille, G.; Mangenot, C.; Lager, I. Spatial density tapered sunflower antenna array. In Proceedings of the 2009 3rd European Conference on Antennas and Propagation, Berlin, Germany, 23–27 March 2009; pp. 778–782.
23. Temiz, M.; Alsusa, E.; Baidas, M.W. A Dual-Functional Massive MIMO OFDM Communication and Radar Transmitter Architecture. *IEEE Trans. Veh. Technol.* **2020**, *69*, 14974–14988. [\[CrossRef\]](#)
24. Zhang, J.A.; Huang, X.; Guo, Y.J.; Yuan, J.; Heath, R.W. Multibeam for joint communication and radar sensing using steerable analog antenna arrays. *IEEE Trans. Veh. Technol.* **2018**, *68*, 671–685. [\[CrossRef\]](#)
25. Ni, Z.; Zhang, J.A.; Huang, X.; Yang, K.; Yuan, J. Uplink sensing in perceptive mobile networks with asynchronous transceivers. *IEEE Trans. Signal Process.* **2021**, *69*, 1287–1300. [\[CrossRef\]](#)
26. Temiz, M.; Alsusa, E.; Baidas, M.W. A Dual-Function Massive MIMO Uplink OFDM Communication and Radar Architecture. *IEEE Trans. Cogn. Commun. Netw.* **2021**, *8*, 750–762. [\[CrossRef\]](#)
27. Spence, T.G.; Werner, D.H. Design of broadband planar arrays based on the optimization of aperiodic tilings. *IEEE Trans. Antennas Propag.* **2008**, *56*, 76–86. [\[CrossRef\]](#)
28. Ma, Y.; Yang, S.; Chen, Y.; Qu, S.W.; Hu, J. High-Directivity Optimization Technique for Irregular Arrays Combined With Maximum Entropy Model. *IEEE Trans. Antennas Propag.* **2020**, *69*, 3913–3923. [\[CrossRef\]](#)
29. Echeveste, J.I.; de Aza, M.Á.G.; Rubio, J.; Craeye, C. Gradient-based aperiodic array synthesis of real arrays with uniform amplitude excitation including mutual coupling. *IEEE Trans. Antennas Propag.* **2016**, *65*, 541–551. [\[CrossRef\]](#)
30. Molisch, A.F. *Wireless Communications*; John Wiley & Sons: Hoboken, NJ, USA, 2012; Volume 34.
31. Richards, M.A.; Melvin, W. *Principles of Modern Radar: Basic Principles*; Institution of Engineering & Technology: London, UK, 2023; Volume 1.
32. Lu, S.; Liu, F.; Hanzo, L. The Degrees-of-Freedom in Monostatic ISAC Channels: NLoS Exploitation vs. Reduction. *IEEE Trans. Veh. Technol.* **2022**, *72*, 2643–2648. [\[CrossRef\]](#)
33. Cai, X.; Miao, Y.; Li, J.; Tufvesson, F.; Pedersen, G.F.; Fan, W. Dynamic mmWave Channel Emulation in a Cost-Effective MPAC With Dominant-Cluster Concept. *IEEE Trans. Antennas Propag.* **2022**, *70*, 4691–4704. [\[CrossRef\]](#)
34. El Ayach, O.; Rajagopal, S.; Abu-Surra, S.; Pi, Z.; Heath, R.W. Spatially sparse precoding in millimeter wave MIMO systems. *IEEE Trans. Wirel. Commun.* **2014**, *13*, 1499–1513. [\[CrossRef\]](#)
35. Nuss, B.; Sit, L.; Fennel, M.; Mayer, J.; Mahler, T.; Zwick, T. MIMO OFDM radar system for drone detection. In Proceedings of the 2017 18th International Radar Symposium (IRS), Prague, Czech Republic, 28–30 June 2017; pp. 1–9.
36. Barneto, C.B.; Riihonen, T.; Turunen, M.; Anttila, L.; Fleischer, M.; Stadius, K.; Ryyänen, J.; Valkama, M. Full-duplex OFDM radar with LTE and 5G NR waveforms: Challenges, solutions, and measurements. *IEEE Trans. Microw. Theory Tech.* **2019**, *67*, 4042–4054. [\[CrossRef\]](#)
37. Schubert, E.; Kunert, M.; Menzel, W.; Fortuny-Guasch, J.; Chareau, J.M. Human RCS measurements and dummy requirements for the assessment of radar based active pedestrian safety systems. In Proceedings of the 2013 14th International Radar Symposium (IRS), Dresden, Germany, 19–21 June 2013; Volume 2, pp. 752–757.
38. Bhardwaj, A.; Caudill, D.; Gentile, C.; Chuang, J.; Senic, J.; Michelson, D.G. Geometrical-empirical channel propagation model for human presence at 60 GHz. *IEEE Access* **2021**, *9*, 38467–38478. [\[CrossRef\]](#)
39. Hersyandika, R.; Miao, Y.; Pollin, S. Guard Beam: Protecting mmWave Communication through In-Band Early Blockage Prediction. In Proceedings of the GLOBECOM 2022—2022 IEEE Global Communications Conference, Rio de Janeiro, Brazil, 4–8 December 2022; pp. 4093–4098. [\[CrossRef\]](#)
40. Virk, U.T.; Haneda, K. Modeling human blockage at 5G millimeter-wave frequencies. *IEEE Trans. Antennas Propag.* **2019**, *68*, 2256–2266. [\[CrossRef\]](#)
41. Zhang, H.; Shi, J.; Zhang, Q.; Zong, B.; Xie, J. Antenna selection for target tracking in collocated MIMO radar. *IEEE Trans. Aerosp. Electron. Syst.* **2020**, *57*, 423–436. [\[CrossRef\]](#)
42. Ramalli, A.; Boni, E.; Savoia, A.S.; Tortoli, P. Density-tapered spiral arrays for ultrasound 3-D imaging. *IEEE Trans. Ultrason. Ferroelectr. Freq. Control* **2015**, *62*, 1580–1588. [\[CrossRef\]](#)
43. Wu, S.; Alrabeiah, M.; Chakrabarti, C.; Alkhateeb, A. Blockage prediction using wireless signatures: Deep learning enables real-world demonstration. *IEEE Open J. Commun. Soc.* **2022**, *3*, 776–796. [\[CrossRef\]](#)

44. Aslan, Y.; Puskely, J.; Roederer, A.; Yarovoy, A. Multiple beam synthesis of passively cooled 5G planar arrays using convex optimization. *IEEE Trans. Antennas Propag.* **2019**, *68*, 3557–3566. [[CrossRef](#)]
45. Grant, M.; Boyd, S.; Ye, Y. CVX: Matlab Software for Disciplined Convex Programming, Version 2.0 Beta. 2013. Available online: <http://cvxr.com/cvx> (accessed on 11 July 2023).

Disclaimer/Publisher’s Note: The statements, opinions and data contained in all publications are solely those of the individual author(s) and contributor(s) and not of MDPI and/or the editor(s). MDPI and/or the editor(s) disclaim responsibility for any injury to people or property resulting from any ideas, methods, instructions or products referred to in the content.